

Enhancement of propagation length of surface plasmons confined in Au nanostripes by QD-PMMA nanocomposite dielectric modes

Isaac Suárez*, Albert Ferrando, Jose Marqués-Hueso, Antonio Díez, Rafael Abargues, Pedro J. Rodríguez-Cantó and Juan P. Martínez-Pastor

UMDO, Instituto de Ciencia de los Materiales, Universidad de Valencia, 46071 Valencia, Spain.

* Corresponding authors: isaac.suarez@uv.es

1. Fabrication details.

1.1. PL and absorbance spectrum of CdSe/ZnS QDs.

The active material used in this work consisted of core-shell CdSe/ZnS quantum dots (QD) [1]. The CdSe core had a radius of 2.5 nm corresponding to an absorption excitonic peak at ≈ 600 nm [2] (blue line in Figure S1). The ZnS shell surrounded the core had a thickness of 1 nm and was grown to decrease surface traps and to increase the emission quantum yield. The Photoluminescence (PL) spectrum (red line in Figure S1) had a Gaussian shape centered at 600 nm with a Full Width at Half Maximum of 40 nm.

According to the results obtained in Ref. [2], when the QDs are embedded in the PMMA matrix there is no a significant alteration of the PL and absorption spectra.

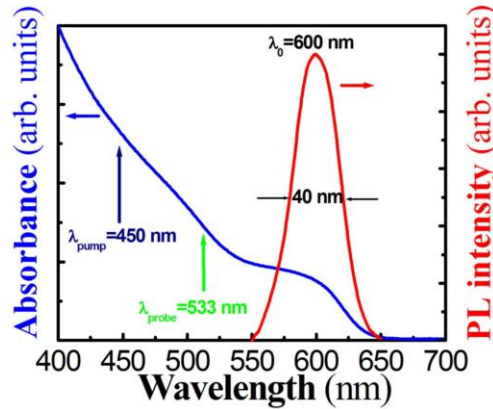


Figure S1. Absorbance (blue line and left axis) and PL (red line and right axis) of the CdSe/ZnS QDs used in this work.

In addition, samples fabricated with CdSe QDs with similar absorbance and PL (see curves in Ref. [2]) were also tested in order to add more consistency to the observed phenomenology reported in the body of the manuscript.

1.2. SEM characterization of Au stripes.

After a standard lift-off process (see methods) Au stripes of 1 μm , 500 nm, 250 nm and 100 nm width were successfully patterned on a SiO_2/Si substrate, as it is presented in the SEM images of Figure S2.

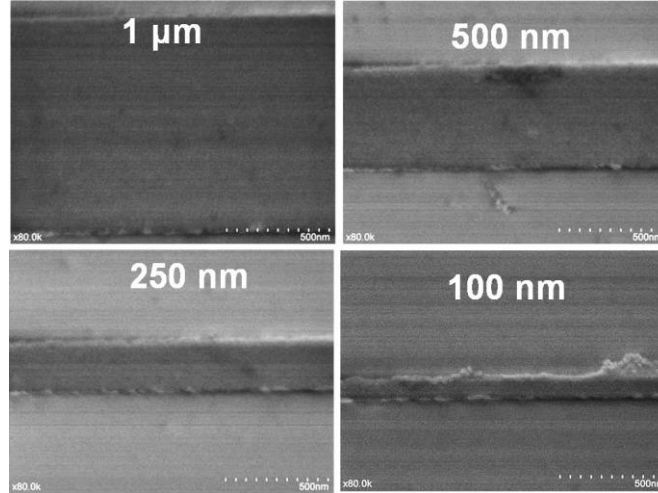


Figure S2. SEM characterization of Au stripes of 1 μm , 500 nm, 250 nm and 100 nm following the process explained in “methods” section.

1.3. Sample preparation.

Au stripes (250 nm - 1 μm wide) were patterned on a SiO_2 (2 μm) /Si substrate (CEMAT Silicon S.A.) by exposing a PMMA layer to a e-beam lithography, and then evaporating 30 nm Au film on the top of the samples followed by an acetone lift-off (see Figure S3). To improve the adhesion of the Au on the SiO_2 4 nm Cr were deposited during the evaporation. After the process straight lines of 2 mm length were well defined on the substrate (see SEM images on Figure S2). Complementary metal structures consisted of planar waveguides fabricated by depositing a 30 nm Au film on the same substrate. In addition, wider Au stripes (4- 20 μm wide) were patterned by using UV-lithography with a SU-8 resist within the lift-off process. Once the plasmonic waveguides are properly fabricated 1 μm thickness of a CdSe-PMMA nanocomposite is spin-coated on the samples and post baked at 80 $^{\circ}\text{C}$ and 150 $^{\circ}\text{C}$ for two minutes each. CdSe colloidal QDs are fabricated following the method develop by Peng's group. The radius was fixed to 2.5 nm to achieve an absorption exciton peak around 580 nm and an emission photoluminescence at 600 nm (Figure S1). Then they were mixed in PMMA with a filling factor of around 10-

3 to obtain the better compromise between PL generation and low propagation losses [2]. Finally samples were cleaved for end fire coupling purposes. Figure S3 presents a cross section of the waveguide structure.

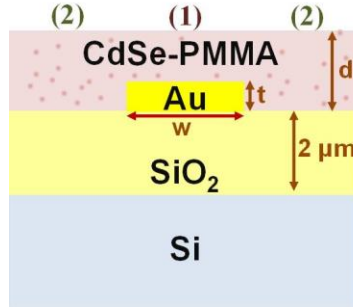


Figure S3. Cross section of the metal-dielectric structures investigated in the present work.

2. Design of planar insulator-metal-insulator (IMI) structures.

2.1. Calculation of effective refractive index and propagation length.

The signal propagating along the waveguide structure depicted in figure S3 was analyzed by solving the propagation constant (the effective refractive index) of the modes supported by the structure. For this purpose the dispersion relation of the modes is obtained by solving Maxwell equations with the appropriate boundary conditions between each interface. Due to the fact that the metal is a lossy material, its permittivity (ϵ_m) is a complex number and with it also the effective refractive index:

$$N_{\text{eff}} = N'_{\text{eff}} + iN''_{\text{eff}} \quad (1)$$

The real part (N'_{eff}) is related with the group velocity of the light, and the imaginary part (N''_{eff}) with the attenuation. Since the damping limits the propagation of the light in plasmonic waveguides, it is useful to define the propagation length as the distance where the intensity of light decays by a factor $1/e$:

$$L = \frac{1}{2 \cdot k_0 \cdot N''_{\text{eff}}} \quad (2)$$

Here k_0 is the wave vector in vacuum ($k_0 = 2\pi/\lambda$) and λ the operation wavelength.

In this work planar waveguides were analyzed by applying the transfer matrix method in a complex plane [4]. The value of the refractive index at the pump (450 nm) and

PL (600 nm) are listed in table S1, and they were obtained from Palick [5] and Johnson and Crysty [6]. It is worth mentioning that the filling factor (ff) of QDs in PMMA is low enough ($\sim 10^{-3}$) to approximate its refractive index to that of PMMA. The coordinate system was chosen by fixing the z axis along the propagation direction, whereas transverse x and y axes are perpendicular and parallel to the Au plane respectively.

Material	405 nm	600 nm
Air	1	1
SiO ₂	1.4696	1.4582
PMMA	1.504	1.489
Au	1.649-0.0065i	0.2203-3i
Si	5.4245-0.2467i	3.9359-0.0193i

Table S1. Material's refractive indexes

2.2. Design of a IMI waveguide.

A planar structure consisted of a Au film surrounded by two semi-infinite dielectric medium (SiO₂ and PMMA) was firstly analyzed in order to establish the influence of the thickness of the metal in the propagating modes (see inset of Figure S4a). This insulator-metal-insulator (IMI) waveguide supports two solutions of bound modes that come from the coupling of the two individual SPP: the Long Range surface Plasmon Polariton (LR-SPP) and the Short Range surface Plasmon Polariton (SR-SPP) [7]. The former mode is characterized by a symmetric shape of the transverse electric field (E_x) and a high localization in the dielectric; while the latter presents an asymmetric shape of E_x and it is strongly confined in the metal (see inset in figure S4a). Therefore, propagation of the SR-SPP signal is strongly limited by the attenuation of the metal, while the losses in the LR-SPP are partially alleviated by the localization of the mode in the dielectric medium. In addition, there is a trade-off between L_p and mode confinement, because the attenuation of modes increases their localization in the metal. The thicker the Au film, the LR-SPP mode is more and more confined in the metal (right axis in Figure S4a), but thick metal films also shorten the L_p of the mode (left axis in Figure S4a). At $\lambda=600$ nm the LR-SPP mode can achieve confinements higher than 5 %, but with a L_p shorter than 2 μm , and for L_p longer than 20 μm the confinement of the mode is reduced down to 2 %. Then, we have

chosen $t=30$ nm as a compromise between both parameters, leading a L_p of $11.4\ \mu\text{m}$ and a confinement of 2.5% .

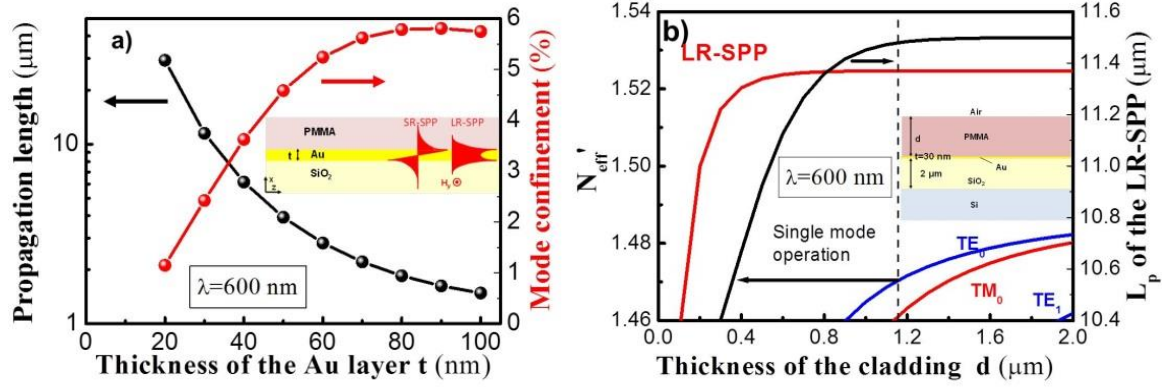


Figure S4. a) Propagation length and confinement factor as a function of the thickness of the Au layer surrounded by semi-infinite dielectrics.) Real part of the effective refractive (left axis) and propagation length (black line and right axis) of the fundamental mode as a function of the thickness of the cladding layer.

Finite dielectrics on the top and the bottom of the metal can influence the propagation of the light along the waveguide. First, a thick enough dielectric can support photonic TE modes, or hybrid photonic-plasmonic TM modes. In the waveguide presented in the inset of Figure S4b, the PMMA propagates TE or TM modes when the cladding is thicker than $d > 0.85\ \mu\text{m}$ and $d > 1.1\ \mu\text{m}$ respectively (see left axis of axis of Figure S4b). Modes in the SiO₂ were not considered since the refractive index of this layer is lower than that in the Si substrate. Indeed, the thickness of SiO₂ was fixed to $2\ \mu\text{m}$ in order to have a good isolation of the light traveling along the waveguide (PMMA or Au) with the Si substrate. Second, the claddings should be thick enough to keep the evanescent tail of the LR-SPP. Therefore the LR-SPP will suffer from a higher attenuation for claddings thinner than $0.4\ \mu\text{m}$, as it is indicated in the right axis of Figure S4b. Then, a cladding of $d=1\ \mu\text{m}$ is thick enough to keep the evanescent tail of the LR-SPP (see blue line in Figure S5a), and to avoid the propagation of light along the PMMA in TM polarization (that could interfere in the measurement). A cladding of $d=1\ \mu\text{m}$, however, confines one (photonic) mode in TE polarization, plotted in Figure S5a with a blue line. In addition, the air/ PMMA/SiO₂ structure constitutes a dielectric waveguide, single mode in both polarizations for the geometrical parameters considered here (see Figure S5b).

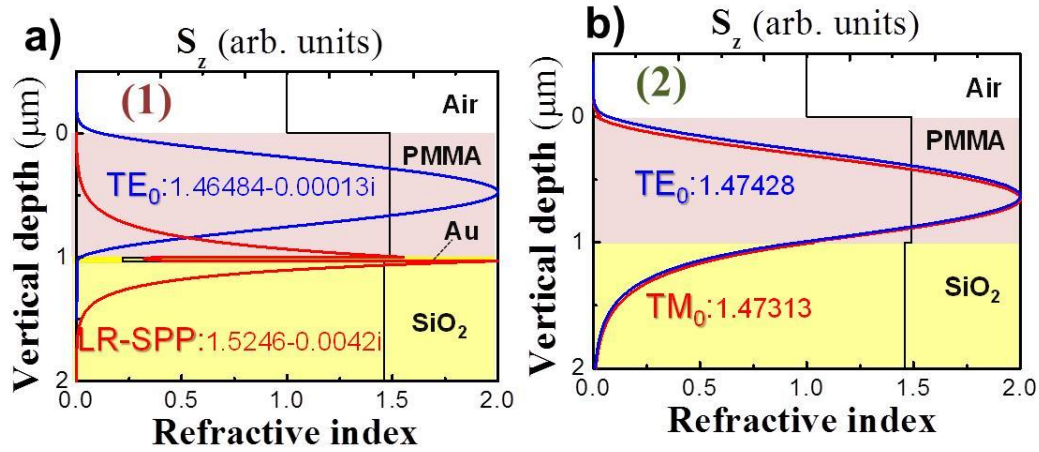


Figure S5. Mode distribution : a) Air/PMMA/Au/SiO₂ and b) Air/PMMA/ SiO₂

3. Profile of the fiber tip

The FTFT was used to selectively excite the QDs in a reduced area of $2\text{-}3\ \mu\text{m}^2$ on the top of the stripes (see Figure S6). The fiber tip was formed by fusion and fast stretching of a standard single-mode optical fiber at 600 nm (SM600, supplied by Thorlabs). The fiber is heated at a given point by an electric arc discharge (electric current 10 mA, duration 750 ms) using a fiber fusion splicer, simultaneously to the application of an appropriate tension. The combined action of heating and fast pulling due to tension reduces the diameter of the fiber until it breaks, leading to the formation of the fiber tip. The tip diameter is $\sim 4\ \mu\text{m}$ and the beam width is typically $2.5\ \mu\text{m}$; the FTFT is robust and does not show optical degradation under normal ambient conditions.

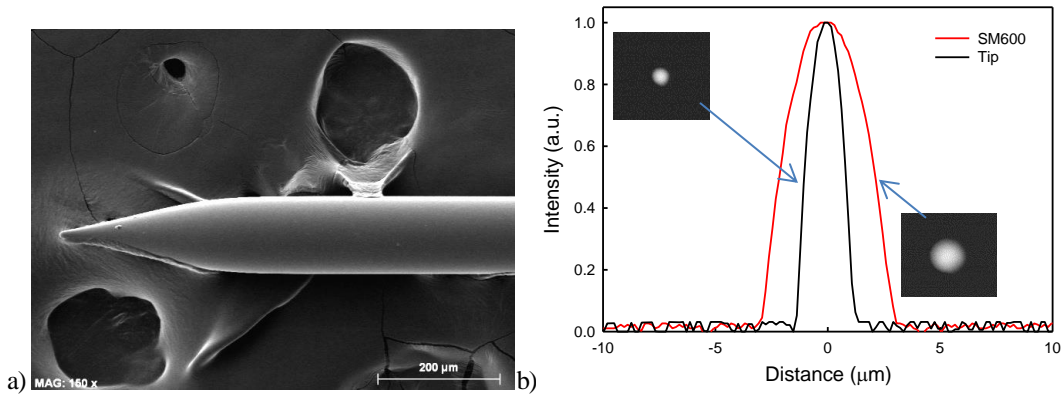


Figure S6. a) SEM image of the tip; b) Profile of the optical beam at the output of the tip (black) and at the output of the SM600 fiber. Inset shows the corresponding near-field intensity patterns.

4. Characterization of the propagation length in planar/microstripes.

In a metal film waveguide the proposed L_p - measuring method yields a single exponential decay, $I_{PL} \propto e^{-z/L_p}$, as observed in Figure S7a, where symbols stand for the experimental data and the continuous line to the exponential decay fitting. For the TM signal in the structure with a planar Au film of $t = 30 \text{ nm}$ a propagation length $L_p = 12 \pm 2 \mu\text{m}$ is deduced, which nicely agrees with the predicted value, $11.4 \mu\text{m}$ (see calculation in section S2). The TE signal exhibits a longer $L_p = 50 \pm 10 \mu\text{m}$, because the mode is confined in the dielectric material capping the metal film, where propagation losses are reduced.

The experimental dependence of the waveguided PL intensity as a function of z in metal stripes surrounded by the active dielectric medium (Figure S3) is shown in Figure S8b for TM (red solid circles) and TE (blue solid circles) modes in the case of a $10 \mu\text{m}$ wide metal stripe. They exhibit a two exponential decay behavior:

$$I_{PL} = A_1 \cdot e^{-z/L_{p1}} + A_2 \cdot e^{-z/L_{p2}} \quad (6)$$

where A_1 and A_2 are constants and L_{p1} and L_{p2} the propagation lengths of the modes in regions 1 and 2 (see Figure S3), respectively. The shortest propagation length, L_{p1} , for the TM mode corresponds to the LR-SPP and is fitted with $L_{p1} = 13 \pm 3 \mu\text{m}$ and $L_{p2} \approx 370 \mu\text{m}$ (red line in Figure S8b). The value of L_{p1} nicely agrees with the calculated one ($11.4 \mu\text{m}$) and it is very close to the value previously obtained for the planar metal-dielectric structure under TM polarization, which is consistent with the large width of the metal stripe. The longest propagation length, $L_{p2} \approx 370 \mu\text{m}$, corresponds to the light travelling out of the metal stripe (regions 2) with a similar dependence under both polarizations TE_0 and TM_0 (see Figure S8b). The fit for the TE_0 mode (blue line in Figure S7b) gives the same value for L_{p2} and a first decay constant $L_{p1} = 50 \pm 10 \mu\text{m}$, which is the same value deduced above for the planar metal-dielectric structure under TE polarization, because this mode is centered at the dielectrics (QD-PMMA nanocomposite). Higher order modes in both regions are forbidden since the thickness of the nanocomposite was set to $d = 1 \mu\text{m}$ (see section S2). The pictures inside Figure S8b compare the near field images at $z=0$ and $z = 200 \mu\text{m}$ for both polarizations; clearly, all plasmonic and photonic modes are present at $z =$

0, whereas only the photonic modes travelling along the dielectric waveguide are still visible (the LR-SPP completely disappears and the TE0 mode is strongly attenuated) for $z = 200 \mu\text{m}$, consistently with their corresponding propagation lengths. It is worth noting that QDs used in the measurements reported in Figure S7 were core-CdSe nanocrystals, but yielded similar results to those presented in the body of the manuscript for core/shell CdSe/ZnS QDs.

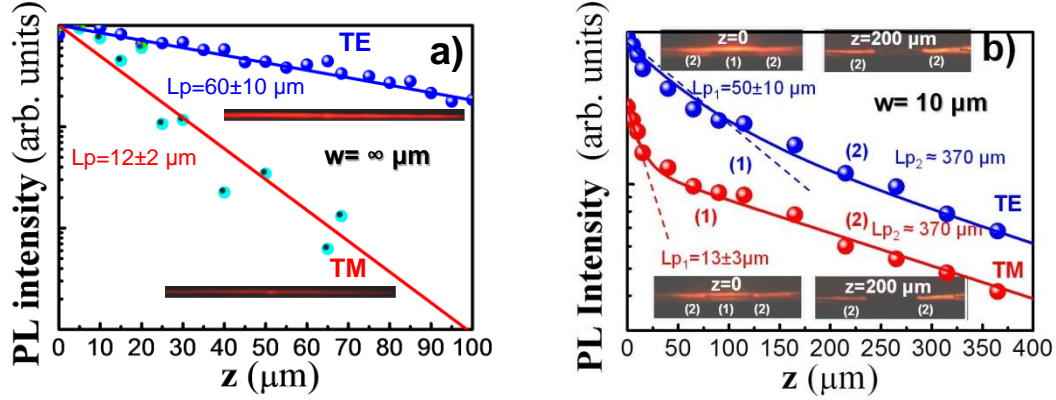


Figure S7. PL as a function of the distance between the stripe and the edge of the sample (z): experimental (data symbols) and fitting curves (continuous lines) for TE (blue color) and TM (red color) polarizations for planar (a) and stripe-like with $w = 10 \mu\text{m}$ (b) metal-dielectric structures.

5. Metal stripes embedded in a dielectric medium.

Modes propagating along the Au and dielectric (PMMA cladding and dielectric waveguide on the left and the right of the stripe) medium constitute a solution of supermodes whose propagation constant can be calculated by a coupling mode theory [4]. Nevertheless, according to the geometry of the system one can consider quasi-plasmonic modes and quasi-photonic modes propagating along the metal and the dielectric, independently. In this way, modes confined in the metal stripe have been calculated by applying the effective index method [4].

The lateral confinement in narrow stripes leads to four fundamental plasmonic supermodes, which are no purely TM [7]. Among these solutions, there is a counterpart bidimensional LR-SPP whose evolution as a function of the stripe width is studied in the text of this work. Insets of Figure S8 depict the fundamental mode distribution for

waveguides of different widths (250 nm, 500 nm and 1 μm). The effective mode area presents a minimum of $2/\lambda^2$ in a range between 200 and 300 nm (red line in the left axis of Figure S8), in agreement with [8]. Therefore, a stripe width of $w=250\text{-}500\text{ nm}$ seems to be optimum since it presents the smaller losses together with the smaller mode area. In addition, the mode confinement is similar to that in the planar film.

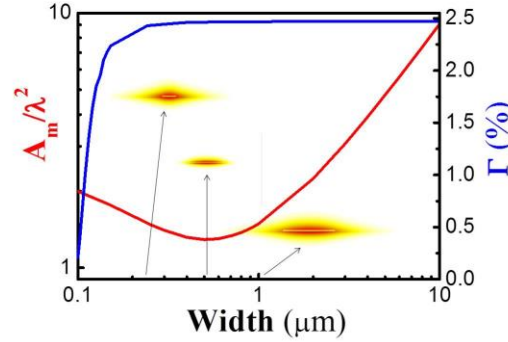


Figure S8. Mode area (red and left axis) and confinement factor (blue and right axis) as a function of the stripe width. Thickness of PMMA and Au were fixed to 1 μm and 30 nm respectively. Inset indicates the Cross section of the LR-SPP mode distribution for different stripes widths

6. Active medium close to metal structures.

The overlap of the mode distribution with the active medium (PMMA layer) indicates the efficiency of coupling of the light emitted by the QDs to a given mode. Following the analysis described in [9], the QDs can be modelled as dipoles located at a distance (r) far to the Au film. Then, coupling efficiency can be calculated by studding the dissipated power in each propagation direction (k_z). The calculations predict a sharp and a broad peak with k_x/k_0 slightly larger than one corresponding to the LR-SPP mode and SR-SPP respectively, as it is presented in Figure S9. Higher and smaller values of the wave vector are related to electron-hole pairs absorbed by the Au layer and coupling to cladding modes respectively. In addition, when the dipole is close to the Au layer, light is mostly coupled to the SR-SPP. However, for distances longer than $r=500\text{ nm}$ the efficiency of coupling to the LR-SPP decreases (see inset in Figure S9), and light is mostly transferred to cladding because the overlap with the mode decreases. Here calculations were performed

by considering the waveguides described in the previous section ($t=30\text{ nm}$ and $d=1\text{ }\mu\text{m}$ and $\lambda=600\text{ nm}$).

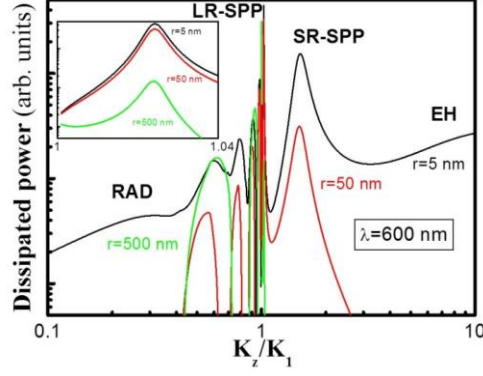


Figure S9. Dissipated power of a as a function of the normalized wave vector for several distances between an emissive dipole and the gold film. $\lambda=600\text{ nm}$

7. Exciton generation in colloidal quantum dots.

The number of electron hole pairs (N_{eh}) per QD was calculated according to the following expression:

$$N_{eh} = \Phi \cdot \sigma_{abs} \quad (3)$$

where Φ is the photon flow and σ_{abs} the absorption cross section. Then the total number of generated excitons (N) was estimated considering the filling factor (ff), i.e., the volume fraction occupied by QDs, and the volume of a QD:

$$N = N_{eh} \cdot \frac{ff}{V} \quad (4)$$

Finally, the gain provided along the waveguide is estimated with the following formula [9]:

$$g = N \cdot \sigma_e \quad (5)$$

where σ_e the emission cross section calculated with the approximation developed in [9]. Then, for the pump fluencies considered here (1 KW/cm^2 was estimated at the input edge of the waveguide by considering a coupling efficiency of 5 %) the lifetime of a QD around 10

ns, and the σ_{abs} calculated from the absorption curve given in [2], the N_{eh} is 0.013, which would provide a gain of 0.16 cm^{-1} for a $ff = 10^{-3}$.

8. Model.

8.1. Hamiltonian of the system.

A simple description of the propagation of pump and signal in the system under consideration is provided by coupled mode theory. We consider the propagation of three modes: the plasmonic component $C_p(\omega_S, z)$ at the signal frequency and the two photonic mode components $C_g(\omega_S, z)$ and $C_g(\omega_P, z)$ at the signal and pump frequencies, respectively. In this approach, the total electric field propagating in the waveguide is approximated by: $\mathbf{E}(x, y, z) \approx C_p(\omega_S, z)\mathbf{e}_p(x, y; \omega_S) + C_g(\omega_S, z)\mathbf{e}_g(x, y; \omega_S) + C_g(\omega_P, z)\mathbf{e}_g(x, y; \omega_P)$, where $\mathbf{e}_p(\omega_S)$ is the amplitude of the uncoupled LR-SPP plasmonic mode at signal frequency whereas $\mathbf{e}_g(\omega_S)$ and $\mathbf{e}_g(\omega_P)$ are the amplitudes of the uncoupled photonic waveguide modes at the signal and pump frequencies, respectively.

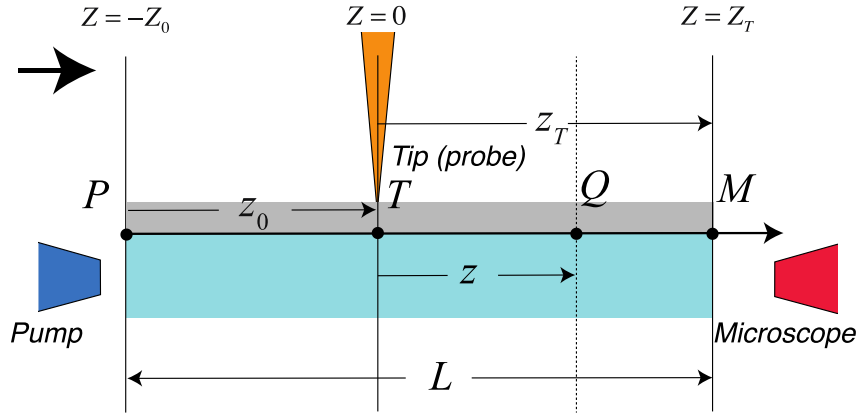


Figure S10. Schematic representation of the experimental situation with its corresponding assignment of relevant points and distances. The origin of the axial distance z is set at tip position T . Pump is represented by point P at a distance z_0 from the tip. Measuring point is M , at a distance z_T from the tip. The total propagation length is given by the axial length of the sample $L = z_0 + z_T$.

By using the vector notation $C(z) = [C_p(\omega_S, z), C_g(\omega_S, z), C_g(\omega_P, z)]^T$, one can write the evolution equation:

$$-i \cdot \frac{dC(z)}{dz} = H \cdot C(z) \quad (7)$$

where the “Hamiltonian” matrix operator is given by

$$H = \begin{bmatrix} \beta_p(\omega_S) & q_g & q'_g \\ q_p & \beta_g(\omega_S) & (2\pi/\lambda_S)\chi(\omega_S, \omega_P) \\ q'_g & (2\pi/\lambda_P)\chi(\omega_P, \omega_S) & \beta_g(\omega_P) \end{bmatrix} \quad (8)$$

and z is the axial distance measured from the tip position (see Figure S11).

In this matrix, $\beta_p(\omega_S)$, $\beta_g(\omega_S)$ and $\beta_g(\omega_P)$ are the propagation constants of the uncoupled SPP and the two waveguide modes, respectively. The q coefficients describe the coupling between the SPP and the photonic mode amplitudes, and the coefficient $\chi(\omega_S, \omega_P)$ is the conversion amplitude of a pump photon into a signal one in the waveguide. A similar interpretation applies to $\chi(\omega_P, \omega_S)$. According to Figure S11, in the absence of tip injection, the pump located at $z = -z_0$ is the only source of photons (C_{PUMP}). In this basis this initial condition is written as:

$$C(-z_0) = \begin{bmatrix} 0 \\ 0 \\ C_{PUMP} \end{bmatrix}. \quad (9)$$

8.2. Solution in the linear regime.

The solution of the matrix coupled mode equations, including the tip source, is naturally given as a linear combination of the three eigenmodes of the coupled system, i.e., the eigenvectors $(\bar{C}_1, \bar{C}_2, \bar{C}_3)$ and eigenvalues $(\beta_1, \beta_2, \beta_3)$ of the coupling matrix H . In the language of waveguide optics these eigenmodes are known as the supermodes of the waveguide structure so that the electric field propagating in the waveguide would be given by a superposition of them. Each supermode propagates with a well-defined propagation constant so its axial dependence is of the type $e^{i\beta_n z}$ with $n = 1, 2, 3$. Nevertheless, in the weak coupling approximation, supermode 1 becomes an SPP-like hybrid mode with $\beta_1 \approx \beta_p(\omega_S)$, whereas supermodes 2 and 3 would be photonic-like with propagation constants similar to those of the uncoupled ones, i.e., $\beta_2 \approx \beta_g(\omega_S)$ and $\beta_3 \approx \beta_g(\omega_P)$. Since our measurements are performed at the signal frequency ω_S , the dominant terms for the detected intensity will be given mostly by the eigenmodes with higher component at frequency ω_S . The measured electric field will be provided essentially by supermodes 1 and

2: $\mathbf{E}(x, y, z) \approx C_1(0)e^{i\beta_1 z}\mathbf{e}_1(x, y) + C_2(0)e^{i\beta_2 z}\mathbf{e}_2(x, y)$, where \mathbf{e}_1 and \mathbf{e}_2 are the electric field distributions of the supermodes 1 and 2. The supermode amplitudes \mathbf{e}_1 , \mathbf{e}_2 and \mathbf{e}_3 can be easily obtained as a linear combination of the amplitudes of the original uncoupled system $\mathbf{e}_p(\omega_S)$, $\mathbf{e}_g(\omega_S)$ and $\mathbf{e}_g(\omega_P)$. This linear combination is provided by the change of basis matrix associated to the diagonalization of the coupling matrix \mathbf{H} .

Another important ingredient in order to describe the system under realistic experimental requirements is the proper choice of initial conditions. Following Figure S11, energy is injected in the system at two different positions: at the pump position P and at the tip position T. The pump at $z = -z_0$ excites supermodes 1,2 and 3, which propagate – uncoupled- until the tip position at $z = 0$. Here, new energy is injected by the probe at the tip, so the initial condition at $z = 0$ has to be modified to take into account this fact. The initial condition at T is then $C_n^P(0) + C_n^T$ for $n = 1,2,3$, where $C_n^P(0) = C_n^P(-z_0)e^{i\beta_n z_0}$ is the component of the supermode n propagated from the pump to the tip and C_n^T is the new amplitude injected by the probe in the n supermode at T. A second propagation of length z_T from T to the measuring point M is then performed. Since we are working in the supermode basis propagation is trivially given by a phase factor:

$$C_n(z_T) = C_n^P(0)e^{i\beta_n z_T} + C_n^T e^{i\beta_n z_T} = C_n^P(-z_0)e^{i\beta_n L} + C_n^T e^{i\beta_n z_T}, \quad (10)$$

where we have taken into account that $L = z_0 + z_T$. Therefore, the field at the right edge of the system (where measurement takes place) will be the sum of the contribution from the pump (at a distance L) and the tip source (at a distance z_T). Consequently, the electric field at the measuring point M in this approximation will be simply given by the superposition $\mathbf{E}(z_T) \approx C_1(z_T)\mathbf{e}_1 + C_2(z_T)\mathbf{e}_2$, which using (10) can be expressed as

$$\mathbf{E}(x, y, z_T) \approx \mathbf{E}^P(x, y, L) + C_1^T e^{i\beta_1 z_T} \mathbf{e}_1(x, y) + C_2^T e^{i\beta_2 z_T} \mathbf{e}_2(x, y). \quad (11)$$

In this expression the first term is nothing but the contribution from the pump and thus it only depends on the sample length L . The second and third terms are the contributions of supermodes 1 and 2 that are excited by the probe at the tip position T. They consequently depend on the distance z_T from the tip to the measuring point.. The corresponding average intensity is $I(z_T) \propto A^{-1} \int dx dy |\mathbf{E}(x, y, z_T)|^2$, where A is the typical measurement area.

The result (11) permits to obtain an expression for $I(z_T)$, which includes many highly oscillating interference terms of the type $\cos[(2\pi/\lambda_S)Re(\beta_n)z_T + \alpha]$. The axial period of these oscillations is of the order of the wavelength, thus of a fraction of a micron, which is considerable smaller than the axial resolution of the experiment, of the order of several microns. These terms naturally average out in the calculation. Writing the supermode propagation constants as $\beta_1=k_0 \cdot n_1 + i \cdot \alpha_1/2$ and $\beta_2=k_0 \cdot n_2 + i \cdot \alpha_2/2$ we find for the average intensity of light at the measuring point

$$I(z_T) \approx I^P(L) + |C_1^T|^2 \cdot e^{-\alpha_1 \cdot z_T} N_1 + |C_2^T|^2 \cdot e^{-\alpha_2 \cdot z_T} N_2 + 2|C_1^T||C_2^T|e^{-\frac{\alpha_1 + \alpha_2}{2} \cdot z_T} |Q_{12}| \cos[k_0(n_2 - n_1)z_T + \gamma], \quad (12)$$

where $N_1 = \int dxdy |\mathbf{e}_1|^2$ and $N_2 = \int dxdy |\mathbf{e}_2|^2$ are normalization integrals and $Q_{12} = \int dxdy \mathbf{e}_1^* \cdot \mathbf{e}_2$ is an intermodal overlapping integral.

The experiment reveals a low axial modulation of the measured intensity as a function of the tip position z_T thus indicating that the interference term is rather small ($|Q_{12}| \ll 1$). Thus, the total intensity of light at the collecting point can be approximated rather well just by a sum of independent intensities in (12):

$$I(z_T) \approx I^P(L) + |C_1^T|^2 \cdot e^{-\alpha_1 \cdot z_T} N_1 + |C_2^T|^2 \cdot e^{-\alpha_2 \cdot z_T} N_2 \quad (13)$$

In the measured intensity the dependences on pump and probe intensities are decoupled. Pump dependence appears only in the term $I^P(L) \propto I_{PUMP}$ and it is absent in the rest since $|C_{1,2}^T|^2 \propto I_{PROBE}$ and α_1 and α_2 cannot have any intensity dependence due to the assumed linear character of the system. Since in the synchronized measurement technique used in the experiment only terms dependent on I_{PROBE} are detected, a good functional form for fitting experimental results is (see equation 3 in the text):

$$I(z_T) = A_1 \cdot e^{-z_T/Lp_1} + A_2 \cdot e^{-z_T/Lp_2} \quad (14)$$

where, according to linear coupled mode theory, $A_1 = |C_1^T|^2 N_1$ and $A_2 = |C_2^T|^2 N_2$. The propagation lengths $Lp_1 = 1/\alpha_1$ and $Lp_2 = 1/\alpha_2$ are thus naturally interpreted as the

propagation lengths of supermodes 1 and 2. Nevertheless, equation (14) does not contain terms directly related to I_{PUMP} . Therefore, the enhancement of L_{p_1} with the pump intensity measured in the experiment cannot be explained by a mechanism based on our assumed linear character of the propagation. The observed experimental dependence of L_{p_1} on I_{PUMP} must be included in the model by some type of nonlinear mechanism associated to the presence of the quantum dots.

8.3. Solution in the nonlinear regime.

The exact nature and origin of the nonlinearity required to explain the observed enhancement of the propagation length of the plasmonic supermode with pump intensity is beyond the scope of this paper. However, we can provide a phenomenological approach to qualitatively explain this enhancement using a nonlinear generalization of the coupled mode theory described in previous section.

In order to define a suitable candidate for the nonlinearity we resort to recent results obtained in photonic nanocomposite QDs waveguides [10]. In these waveguides, which can be considered equivalent to the ones studied here when the metal layer is absent, it is possible to achieve a change in the effective refractive index of the mode at the signal frequency when the active medium is strongly and efficiently pumped at the pump frequency. This phenomenon can be explained in terms of coherent population oscillations by using a four-wave mixing description [11]. In our case, the nonlinearity of the phenomenon would be attributed to the presence of QDs in the nanocomposite waveguide. In our coupled mode model, represented by the Hamiltonian (8), this type of nonlinear modulation would be given by adding an extra term of the form $(\frac{2\pi}{\lambda_s})|C_g(\omega_p, z)|^2$ to the propagation constant of the waveguide mode at the signal frequency $\beta_g(\omega_s)$. This term effectively will change the effective refractive index of the waveguide mode at ω_s if the intensity of the pump is modified since $|C_g(\omega_p, z)|^2 \propto I_{\text{PUMP}}$.

In our description of the problem using the linear supermodes of the waveguide the linear Hamiltonian is diagonal. In the supermode basis, a nonlinear term of this type would generate nonlinear terms for all the matrix elements of the nonlinear H since both $C_g(\omega_s, z)$

and $C_g(\omega_P, z)$ are linear combinations of the supermode components C_n . However, not all the nonlinear terms would be equally important. We can use a physical argument to determine the dominant terms. Since supermodes 2 and 3 are essentially given by the photonic-like waveguides modes at the signal and pump frequency, respectively, we expect the most important dominant term to be a modification of β_2 of the form $(\frac{2\pi}{\lambda_S})|C_3|^2$. However, this term alone could not explain the intensity dependence of β_1 experimentally observed since some type of coupling between supermodes 2 and 1 would be required. Since, by definition, supermodes 1 (photonic-like) and 2 (plasmonic-like) are uncoupled in the linear regime, the second expected dominant term should be a nonlinear coupling term between the photonic supermode 2 and the plasmonic supermode 1. All in all, we introduce the following nonlinear generalization of the Hamiltonian H in the supermode basis considering only these two dominant terms and neglecting the rest:

$$H^{NL} = \begin{bmatrix} \beta_1 & \gamma_{12}(\frac{2\pi}{\lambda_S})|C_2|^2 & 0 \\ 0 & \beta_2 + \gamma_{23}(\frac{2\pi}{\lambda_S})|C_3|^2 & 0 \\ 0 & 0 & \beta_3 \end{bmatrix}. \quad (15)$$

Using this nonlinear Hamiltonian we will see that we can provide a qualitative explanation of the observed response in the pump intensity by adjusting the nonlinear parameters, which in all cases should be small as compared to the linear ones. By performing a number of simulations we have recognized that an important property to find a substantial nonlinear response in supermode 1, when most of the initial pumping goes to supermode 3, is that β_1 and the effective propagation constant of supermode 2, including the nonlinear contribution, are close to resonance condition. Since the nonlinear coefficient γ_{23} has to be necessarily small, this fact implies that the real parts of the linear propagation constant β_1 and β_2 cannot be too different. Equivalently, the original effective refractive indices of the LR-SPP and the waveguide mode at the signal frequency should be similar. This fact guides our choice of the physical parameters included in the original non-diagonal linear Hamiltonian (8).

We performed numerical simulations using the nonlinear Hamiltonian (15) that reproduce the two propagation scheme associated to the existence of two injection points, as reflected

in Figure S10. We reproduce the propagation procedure followed in the linear case and explained in 5.2. First, we propagate the initial state (9), written in the supermode basis, from the pump point P to the tip position T, i.e, from $z = -z_0$ to $z = 0$. Propagation is no longer trivial, not even in the supermode basis, since the nonlinear terms in (15) couple light among the three supermodes in a non-trivial way. Once the supermode components are evaluated at $z = 0$, a new initial condition is set, as in the linear case, by adding the tip injection component to the propagated one from the pump: $C_n^P(0) + C_n^T$. A second nonlinear propagation is then performed to calculate the final supermode components at the measuring point M located at $z = z_T$. This permits to evaluate the ratio $I_1(z_T)/I_1(0)$ associated to the plasmonic supermode 1.

As we have seen in 5.2, in the linear case this ratio is independent of any injected intensity: $I_1^{LIN}(z_T)/I_1^{LIN}(0) = e^{-z_T/Lp_1}$, so that in logarithmic scale its representation is a straight line with negative slope $-\alpha_1 = -1/Lp_1$ (red curve in Figure S12). In Figure S12 we represent the value of the same ratio using our minimal nonlinear generalized model for two different pump intensities and for a fixed probe intensity. The ratio between them is 1100:96:26, which follows the proportion of the experimental ones. The election of physical parameters is the following. For the propagations constants we choose $\beta_p(\omega_S) = (2\pi/\lambda_S)1.51 + (1/40)i \text{ (}\mu\text{m}^{-1}\text{)}$, $\beta_g(\omega_S) = (2\pi/\lambda_S)1.50 + (1/400)i \text{ (}\mu\text{m}^{-1}\text{)}$ and $\beta_g(\omega_P) = (2\pi/\lambda_P)1.50 + (1/400)i \text{ (}\mu\text{m}^{-1}\text{)}$, so that the condition of proximity between n_1 and n_2 is satisfied (n_3 being slightly greater than n_2 , as expected for the mode of a dielectric waveguide at a bit larger frequency.) Their imaginary parts are chosen to lead to attenuation coefficients close to the experimental values for supermodes 1 and 2 ($\alpha_1 \sim 2\text{Im}[\beta_p(\omega_S)]$ and $\alpha_2 \sim 2\text{Im}[\beta_g(\omega_S)]$) obtained in the absence of pumping, i.e., when the system behaves essentially linear. For the linear coupling coefficients we select $q_g = (2\pi/\lambda_S)0.005 \text{ (}\mu\text{m}^{-1}\text{)}$ and for the conversion amplitude $\chi(\omega_S, \omega_P) = 0.1$. The rest of linear coupling coefficients are set to zero. This choice permits a good agreement with experimental results in the absence of pumping, which is the case when the linear analysis in 5.2 is valid and equations (13) and (14) can be applied after diagonalization of the linear Hamiltonian (8). The second step is to find, provided they exist, values for the nonlinear coefficients γ_{12} and γ_{23} , which can lead to a pump intensity dependent ratio $I_1(z_T)/I_1(0)$

qualitatively compatible with experimental results. For values $\gamma_{12} = 8 \cdot 10^{-4}$ and $\gamma_{23} = 5.8 \cdot 10^{-5}$ we obtain the dotted green and blue curves in Figure S11 showing a significant increase in the effective propagation length, as compared to the linear case, for pump intensities following the experimental ratio 1100:96. Similar behavior can be found for values of nonlinear coefficients of the same order of magnitude.

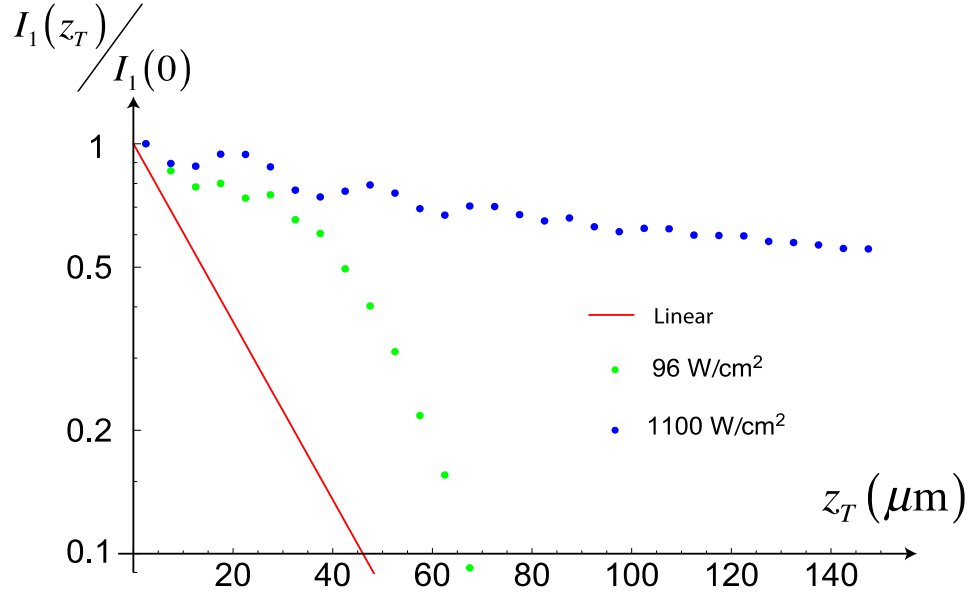


Figure S11. Normalized intensity for the plasmonic supermode 1 as a function of the tip position z_T . Results are obtained by solving coupled mode theory using the nonlinear Hamiltonian (15) for different levels of pump intensity. The red curve represents the linear case ($\gamma_{12} = 0$ and $\gamma_{23} = 0$) after averaging high frequency axial oscillations. The green and dotted curves represent the normalized intensity obtained in the nonlinear case for a value of the pump intensity of 96 and 1100 W/cm^2 , respectively.

8.4. Generation of PL under two-photon absorption.

Colloidal CdSe/ZnS QDs used in this work presented emission under two photon absorption when the nanostructures were pumped with a Ti:sapphire laser at 800 nm (76 MHz, 100 fs). Figure S12 shows the PL generated by this non-linear mechanism where the intensity exhibits a superlinear increase with the pump power (see inset in the Figure).

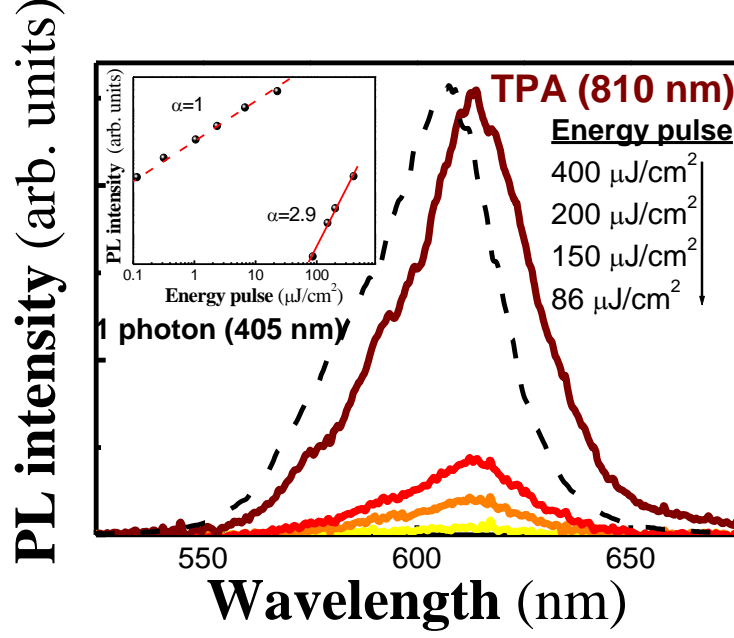


Figure S12. PL spectra under two-photon absorption. The inset plots the intensity of PL as a function of the pump energy revealing a superlinear increase.

8.5. Effective gain and enhancement factor.

Our results in previous section show that a proper nonlinear mechanism can explain the observed enhancement with pump intensity of the plasmonic supermode propagation length. This fact is quantitatively reflected in Figure S12, in which our nonlinear model predicts that $I_1(z_T)$ is indeed dependent on I_{PUMP} . In order to find a proper and experimentally operative way to characterize this effect in the propagation of the plasmonic supermode we introduce a characteristic parameter closely linked to $I_1(z_T, I_{PUMP})$. We define an effective I_{PUMP} -dependent attenuation coefficient $\alpha_{1,eff}(z_T, I_{PUMP})$ for the plasmonic supermode 1 in the following way:

$$\frac{dI_1(z_T, I_{PUMP})}{dz_T} = -\alpha_{1,eff}(z_T, I_{PUMP}) \cdot I_1(z_T, I_{PUMP}) \quad (16)$$

From Figure S12 it is clear that due to the oscillating behavior in z_T of I_1 for non-zero pumping, this effective attenuation coefficient is necessarily axially inhomogeneous. This is in contrast to the linear case (red curve in Figure S11), which according to equation (13), would be given by:

$$\frac{dI_1(z_T)}{dz_T} = -\alpha_1 \cdot I_1(z_T) \quad (17)$$

where α_1 is the z_T -independent attenuation coefficient of the linear plasmonic supermode. This constant is trivially related to its associated propagation length $\alpha_1=1/Lp_1$, and it is obtained experimentally by fitting the measured intensities (with no pump) to the dependence on z_T predicted by theory in (14).

If, as is the case in our experiment, the I_{PUMP} -dependent effective coefficient for supermode 1, $\alpha_{1,\text{eff}}(z_T, I_{PUMP})$, is consistently smaller than α_1 for all z_T we can write:

$$\alpha_{1,\text{eff}}(z_T, I_{PUMP}) = \alpha_1 - g_1(z_T, I_{PUMP}) \quad (18)$$

where $g_1(z_T, I_{PUMP}) > 0$ can be interpreted as the effective gain induced in the plasmonic supermode 1 by the simultaneous effect of modal coupling, conversion and induced nonlinearity due to QDs. The effective propagation length of the plasmonic supermode would be, as usual:

$$Lp_{1,\text{eff}}(z_T, I_{PUMP}) = \frac{1}{\alpha_{1,\text{eff}}(z_T, I_{PUMP})} = \frac{1}{\alpha_1 - g_1(z_T, I_{PUMP})} > Lp_1 = \frac{1}{\alpha_1} \quad (19)$$

Using the results for $I_1(z_T)$ provided by our nonlinear generalization of coupled mode theory it is possible to evaluate the particular dependence on z_T of the effective propagation length or, alternatively, of the effective gain. Despite in the nonlinear case $Lp_{1,\text{eff}}$ and $\alpha_{1,\text{eff}}$ are inhomogeneous functions of the tip position z_T , as one can clearly see in Figure S12 where green and blue dotted curves differ from a straight line, it is possible to define axial average values for the whole sample of length L for both $Lp_{1,\text{eff}}$ and $\alpha_{1,\text{eff}}$. For the effective attenuation coefficient $\alpha_{1,\text{eff}}$ we define its axial average as

$$\overline{\alpha_{1,\text{eff}}(I_{PUMP})} = L^{-1} \int_0^L dz_T \alpha_{1,\text{eff}}(z_T, I_{PUMP}) \quad (20)$$

and the average effective propagation length, $\overline{Lp_{1,\text{eff}}}$, as its inverse. The average effective gain would be simply given by the average version of (18): $\overline{\alpha_{1,\text{eff}}(I_{PUMP})} = \alpha_1 - \overline{g_1(I_{PUMP})}$. These I_{PUMP} -dependent average quantities compare more easily to experimental values. Experimentally, we can fit the expression for the total intensity $I(z_T)$

at the signal frequency (14) to measured values, in order to estimate $\overline{\alpha_{1,\text{eff}}} = 1/\overline{Lp_{1,\text{eff}}}$ for different levels of pump intensity. These fitted values can be also understood as an axial average of the propagation length for the entire sample length L. The axial average of the effective attenuation coefficient $\overline{\alpha_{1,\text{eff}}}$ can be obtained as well by integrating equation (16) over the sample length L to obtain the simple expression:

$$\overline{\alpha_{1,\text{eff}}}(I_{\text{PUMP}}) = \overline{Lp_{1,\text{eff}}}(I_{\text{PUMP}})^{-1} = -\frac{1}{L} \ln \left[\frac{I_1(L; I_{\text{PUMP}})}{I_1(0; I_{\text{PUMP}})} \right] \quad (21)$$

References

- [1] Reiss P.; Protière M.; Li L., *Small* 5, 154 (2009).
- [2] Suárez I.; Gordillo H.; Abargues R.; Albert S.; Martínez-Pastor J. P., *Nanotechnology* 22, 435202 (2011).
- [3] Arques L.; Carrascosa A.; Zamora V.; Díez A.; Cruz J. L.; Andrés M. V. *Opt. Lett.* 2011, 36, 3452-3454
- [4] Ginés Lifante, *Integrated Photonics. Fundamentals*, Ed. John Wiley & Sons (2003)
- [5] Palik E.D. *Handbook of optical constants of solids*. Elsevier, 1997.
- [6] Johnson P. B.; Christy R. W. *Phys. Rev. B* **1972**, 6, 4370-4379
- [7] Berini P *Adv. Opt. Photonics* 2009, 1, 484-588
- [8] Oulton R. F.; Sorger V. J.; Genov D. A.; Pile D. F. P., Zhang X. *Nat. Photonics* 2008, 2, 496-500
- [9] Barnes W. L. *J. Mod. Opt.* **2009**, 45, 661-699
- [10] Hervás J.; Suárez I.; Pérez J.; Rodríguez Cantó P. J.; Abargues R.; Martínez-Pastor J.P.; Sales S.; Capmany J. *Opt. Express* 2015, 23, 14351-14359
- [11] Mecozzi A.; Mork j.; Hofmann M. *Opt. Lett.* 2005, 21, 1017-1019